

DRAFT VERSION OCTOBER 13, 2018

Preprint typeset using L^AT_EX style AASTeX6 v. 1.0

MULTIPLE GAPS WITH LARGE GRAIN DEFICIT IN THE PROTOPLANETARY DISK AROUND TW HYA

TAKASHI TSUKAGOSHI¹, HIDEKO NOMURA², TAKAYUKI MUTO³, RYOHEI KAWABE⁴, DAIKI ISHIMOTO^{2,5},
KAZUHIRO D. KANAGAWA⁶, SATOSHI OKUZUMI², SHIGERU IDA⁷, CATHERINE WALSH⁸, TOM J. MILLAR⁹

¹College of Science, Ibaraki University, Bunkyo 2-1-1, Mito, Ibaraki, 310-8512, Japan;
takashi.tsukagoshi.sci@vc.ibaraki.ac.jp

²Department of Earth and Planetary Sciences, Tokyo Institute of Technology, 2-12-1 Ookayama, Meguro, Tokyo, 152-
8551, Japan

³Division of Liberal Arts, Kogakuin University, 1-24-2 Nishi-Shinjuku, Shinjuku-ku, Tokyo, 163-8677, Japan

⁴National Astronomical Observatory of Japan, 2-21-1 Osawa, Mitaka, Tokyo 181-8588, Japan

⁵Department of Astronomy, Graduate School of Science, Kyoto University, Kitashirakawa-Oiwake-cho, Sakyo, Kyoto,
606-8502, Japan

⁶Institute of Physics and CASA*, Faculty of Mathematics and Physics, University of Szczecin, Wielkopolska 15, 70-451
Szczecin, Poland

⁷Earth-Life Science Institute, Tokyo Institute of Technology, 2-12-1 Ookayama, Meguro, Tokyo 152-8550, Japan

⁸Leiden Observatory, Leiden University, P. O. Box 9513, 2300 RA Leiden, The Netherlands

⁹Astrophysics Research Centre, School of Mathematics and Physics, Queen's University Belfast, University Road,
Belfast BT7 1NN, UK

ABSTRACT

We report ~ 3 au resolution imaging observations of the protoplanetary disk around

arXiv:1605.00289v1 [astro-ph.SR] 1 May 2016

TW Hya at 138 and 230 GHz with the Atacama Large Millimeter/Submillimeter Array. Our observations revealed two deep gaps ($\sim 25\text{--}50\%$) at 22 and 37 au and shallower gaps (a few %) at 6, 28, and 44 au, as recently reported by [Andrews et al. \(2016\)](#). The central hole with a radius of ~ 3 au was also marginally resolved. The most remarkable finding is that the power-law index of the dust opacity β , derived from the spectral index α between bands 4 and 6, peaks at the 22 au gap with $\beta \sim 1.7$ and decreases toward the disk center to $\beta \sim 0$. Our model fitting suggests that the overall disk structure can be reproduced with the inner hole and the gaps at 22 and 37 au. The most prominent gap at 22 au could be caused by the gravitational interaction between the disk and an unseen planet with a mass of $\lesssim 1.5 M_{\text{Neptune}}$ although other origins may be possible. The planet-induced gap is supported by the fact that β is enhanced at the 22 au gap, indicating a deficit of \sim mm-sized grains within the gap due to dust filtration by a planet. Alternatively, the destruction of large dust aggregates due to the sintering of major volatiles might cause the multiple ring structure. We also find weak sinusoidal patterns with wavelengths of 5–10 au, which may be related to dynamical instabilities within the disk.

Keywords: protoplanetary disks — stars: individual(TW Hya)

1. INTRODUCTION

Protoplanetary disks are the birthplaces of planets. The complex structures of protoplanetary disks such as spiral arms, inner holes, and gap and ring, recently reported by high-resolution infrared observations ([Akiyama et al. 2015](#); [Muto et al. 2012](#); [Tsukagoshi et al. 2014](#)), are believed to be potential evidence of unseen planets in the disk. Most recently, high-resolution observations with the ALMA have found multiple gaps and rings in a disk even at submillimeter wavelengths ([ALMA](#)

Partnership et al. 2015). Since submillimeter emission better traces the midplane density structures than infrared, the gaps and rings are thought to be direct evidence of the absence and enhancement of disk material, and therefore related to the planet formation process. The origin of multiple gaps and rings is still under debate: several theoretical studies predict a formation scenario due to material clearance by planets (Tamayo et al. 2015; Kanagawa et al. 2015), replenishment of small dust grains by sintering of molecules (Okuzumi et al. 2016), or secular gravitational instability (Takahashi & Inutsuka 2014).

TW Hya is a $0.8 M_{\odot}$ T Tauri star surrounded by a disk at a distance of ~ 54 pc (e.g., Andrews et al. 2012). Since the disk is almost face-on with an inclination angle of 7° (Qi et al. 2004), TW Hya is one of the best astronomical laboratories to investigate the radial structure of protoplanetary disks. The disk mass has been measured to be $> 0.05 M_{\odot}$ from HD line observations by the *Herschel* Space Observatory, indicating that it is massive enough to form a planetary system (Bergin et al. 2013). Recently, a gap in the dust emission has been found at 20–30 au by submillimeter and near infrared observations (Akiyama et al. 2015; Nomura et al. 2016), which is possibly associated with the CO snow line (Qi et al. 2013). Most recently, Andrews et al. (2016) reported the existence of multiple, axisymmetric annuli at 22, 37, and 43 au at a spatial resolution of ~ 1 au. The depth and width of the submillimeter gap at 20–30 au is consistent with clearing by a super-Neptune mass planet (Nomura et al. 2016). However, no clear consensus has been reached yet on the origin of the gap due to the lack of corresponding information on the dust size distribution with the comparable spatial resolution. In this paper, we report multi-frequency observations of the disk around TW Hya with ALMA to probe the detailed disk structure and the change of dust spectral index across the dust gaps and rings at a spatial resolution of ~ 3 au.

2. OBSERVATIONS

High-resolution continuum observations at bands 4 and 6 (138 and 230 GHz) with the ALMA were carried out on 2015 December 1 and 2 (2015.A.00005.S). In the observation period, 36 of the 12-m antennas were operational and the antenna configuration was in transition from C36-7 to C36-1, resulting in maximum baselines of 6.5 and 10.4 km for band 4 and 6, respectively. We employed the Time Division Mode of the correlator, which is optimized for continuum observations. The correlator was configured to detect dual polarizations in 4 spectral windows with a bandwidth of 1.875 GHz each, resulting in a total bandwidth of 7.5 GHz for each observed band. The amplitude and phase were calibrated by observations of a quasar J1103-3251, and J1037-2934 was used for absolute flux calibration. The observed passbands were calibrated by 5 min observations of J1037-2934 and J1107-4449 for band 4 and 6, respectively.

The visibility data were reduced and calibrated using the Common Astronomical Software Application (CASA) package, version 4.5.0. After flagging bad data and applying the calibrations for bandpass, complex gain, and flux scaling, the corrected visibilities were imaged by the CLEAN algorithm. The visibilities at band 6 with uv lengths >3000 k λ were flagged out because of significant phase noise. The uv sampling for baseline $\lesssim 200$ k λ was particularly sparse along the north-south direction (i.e., v axis of the uv coverage) for both bands 4 and 6 data. This causes artificial structure in the resultant image due to false reconstruction by the CLEAN deconvolution method. We have downloaded band 6 archival data (2012.1.00422.S; PI: K. Öberg), in which the maximum baseline is 650 m (~ 500 k λ), these data were combined with our band 6 data after fixing the phase center. There were no available short-baseline data at band 4, hence only the long-baseline data were used for imaging. The obtained band 4 image appears similar to that with the band 6 image, however, there is slight asymmetry in the intensity distribution at band 4. To improve the image fidelity, we performed the iterative self-calibration imaging for each band data using the initial CLEAN image as a model image.

Using all of the corrected visibilities after the iterative self-calibration imaging, we constructed a combined image of the band 4 and 6 (190 GHz) data with the multi-frequency synthesis (MFS) method and taking into account the spectral index ($nterm=2$ in CASA *CLEAN* task). Briggs weighting with $robust=0.0$ was employed for the deconvolution, and we also employed the multiscale option with scale parameters of 0, 5, and 15 for better reconstruction of extended emission. The achieved spatial resolution of the combined image is 72.7×47.8 mas, with a position angle of $52^\circ.9$, corresponding to 3.9×2.9 au. The noise level is $15.7 \mu\text{Jy beam}^{-1}$.

3. RESULTS

Figure 1(a) shows the combined image of the band 4 and 6 data with the MFS method (hereafter MFS image). The MFS image shows circular symmetric multiple gaps and rings. In addition, we have resolved an inner hole with radius ~ 3 au as predicted from analysis of the spectral energy distribution (Calvet et al. 2002). The total flux density is 386.3 ± 0.6 mJy at 190 GHz ($\text{SN} \sim 150$), which agrees well with the previous estimation at submillimeter wavelengths (Qi et al. 2004; Andrews et al. 2012). There is no appreciable deviation from circular symmetry in the gaps. To confirm the gap structures, we plot the deprojected radial profile in figure 1(c). There are two prominent gaps at 22 and 37 au, and relatively weak decrements of the surface brightness are also seen at 6, 28, and 44 au. These observed features agree with those found by recent high-resolution (~ 1 au) observations at band 7 (Andrews et al. 2016).

Figure 1(b) shows the spatial variation of the spectral index α (see eq. (2) for definition). The obtained spectral index map is highly non-axisymmetric, and it is likely to be artificial due to the remaining sparse uv coverage < 200 k λ along the v-axis at band 4. To check the uncertainty, we plot the deprojected radial profiles over different azimuthal angles in figure 1(d); the averaging over full azimuth, position angles from 60° to 120° and from 240° to 330° (East-West direction), and position

angles from -30° to 30° and from 150° to 210° (North-South direction). The derived profiles are different, implying that the sparse uv coverage <200 k λ causes uncertainty in the value of α especially at larger radii. Additional observations to gain better uv coverage at short baselines in band 4 are required to obtain a better quality map of α . The EW direction data is the most reliable because the sparse uv distribution appears roughly along the north-south direction and because the intensity-weighted mean value of the spectral index agrees well with a previous measurement for the entire disk (Pinilla et al. 2014). Hence, we use the EW direction data in all subsequent analysis, and the shadows in figure 1(b) indicate locations where the value of α is expected to be unreliable.

The intensity $I_\nu(R)$ and the spectral index $\alpha(R)$ are related to the dust temperature $T_d(R)$, the optical depth $\tau_\nu(R)$, and dust opacity index $\beta(R)$ by

$$I_\nu(R) = B_\nu(T_d(R)) (1 - \exp[-\tau_\nu]) \quad (1)$$

and

$$\alpha(R) \equiv \frac{d \log(I_\nu)}{d \log \nu} = 3 - \frac{T_0}{T_d(R)} \frac{e^{T_0/T_d(R)}}{e^{T_0/T_d(R)} - 1} + \beta(R) \frac{\tau_\nu(R)}{e^{\tau_\nu(R)} - 1}. \quad (2)$$

Here, $B_\nu(T)$ is the Planck function, h is Planck's constant, c is the speed of light and $T_0 = h\nu/k_B$ where k_B is Boltzmann's constant. If we assume one of $T_d(R)$, $\tau_\nu(R)$, or $\beta(R)$, it is possible to derive the other two parameters from the MFS data. Here, we assume that $T_d(R)$ is given by $T_d(R) = T_{10}(R/10 \text{ AU})^{-0.3}$ and vary T_{10} from 22 to 30 K. This assumption is based on the fitting of the model result in Andrews et al. (2012), where $T_{10} \sim 22$ K is the best fit value. We use several different temperatures to see how temperature affects the derived physical quantities. We restrict ourselves to $T_{10} > 20$ K because otherwise the gas temperature would fall below the brightness temperature in the inner regions ($R \lesssim 10$ au).

Figure 2 shows the radial profiles of the optical depth τ and the opacity index β . The disk is optically thin at $R > 15$ au in all the cases and marginally optically thick in the inner part. This is in

contrast with HL Tau (ALMA Partnership et al. 2015; Pinte 2016), where an optically thick region extends to much larger radii $R \lesssim 40$ au. We see a prominent drop in the optical depth at $R < 5$ au, which likely corresponds to the inner hole (Calvet et al. 2002). The optical depth profiles have two dips at $R \sim 22$ au and ~ 37 au.

One of the most remarkable feature of the β profile is the peak at ~ 22 au, which is exactly the location of the gap in the surface brightness profile. This is strong evidence that small dust grains are more abundant within the gap than at other locations in the disk. Overall, the opacity index β increases from ~ 0 to ~ 1.7 with radius up to ~ 20 au, beyond which the estimate of β may be affected by the uncertainties in α discussed in the previous section. Radially increasing profiles of β are also seen in other T Tauri disks (Pérez et al. 2012).

We note that it is possible to derive $T_d(R)$ and $\tau(R)$ by assuming $\beta(R)$ or to derive $\beta(R)$ and $T_d(R)$ by assuming $\tau(R)$. To confirm that $\tau(R)$ really has a gap and/or β increases within the gap, additional data from several different bands are necessary.

4. DISCUSSION

4.1. Structures of the Disk and Gaps

To quantify the gap width and depth, we fit the radial profiles of the optical depth $\tau(R)$ using a model that has an inner hole and two gaps centered at ~ 22 and ~ 37 au. We assume that the background profile is given by a power-law with index g , $\tau_{\text{bg}} = \tau_0(R/10 \text{ au})^{-g}$, and the shape of the gap is assumed to be Gaussian with a depth relative to background, A_g , position r_g and width, w_g ,

$$f_{\text{gap}} = 1 + (10^{A_g} - 1) \exp \left[-\frac{(R - r_g)^2}{w_g^2} \right]. \quad (3)$$

We use three Gaussian functions to represent the inner hole, where r_g is fixed to zero, and the two deepest gaps at 22 and 37 au, i.e., we fit the radial profiles of $\tau(R)$ by the function

$$\tau_{\text{model}}(R) = \tau_{\text{bg}}(R) \times f_{\text{gap,in}} \times f_{\text{gap,22au}} \times f_{\text{gap,37au}}. \quad (4)$$

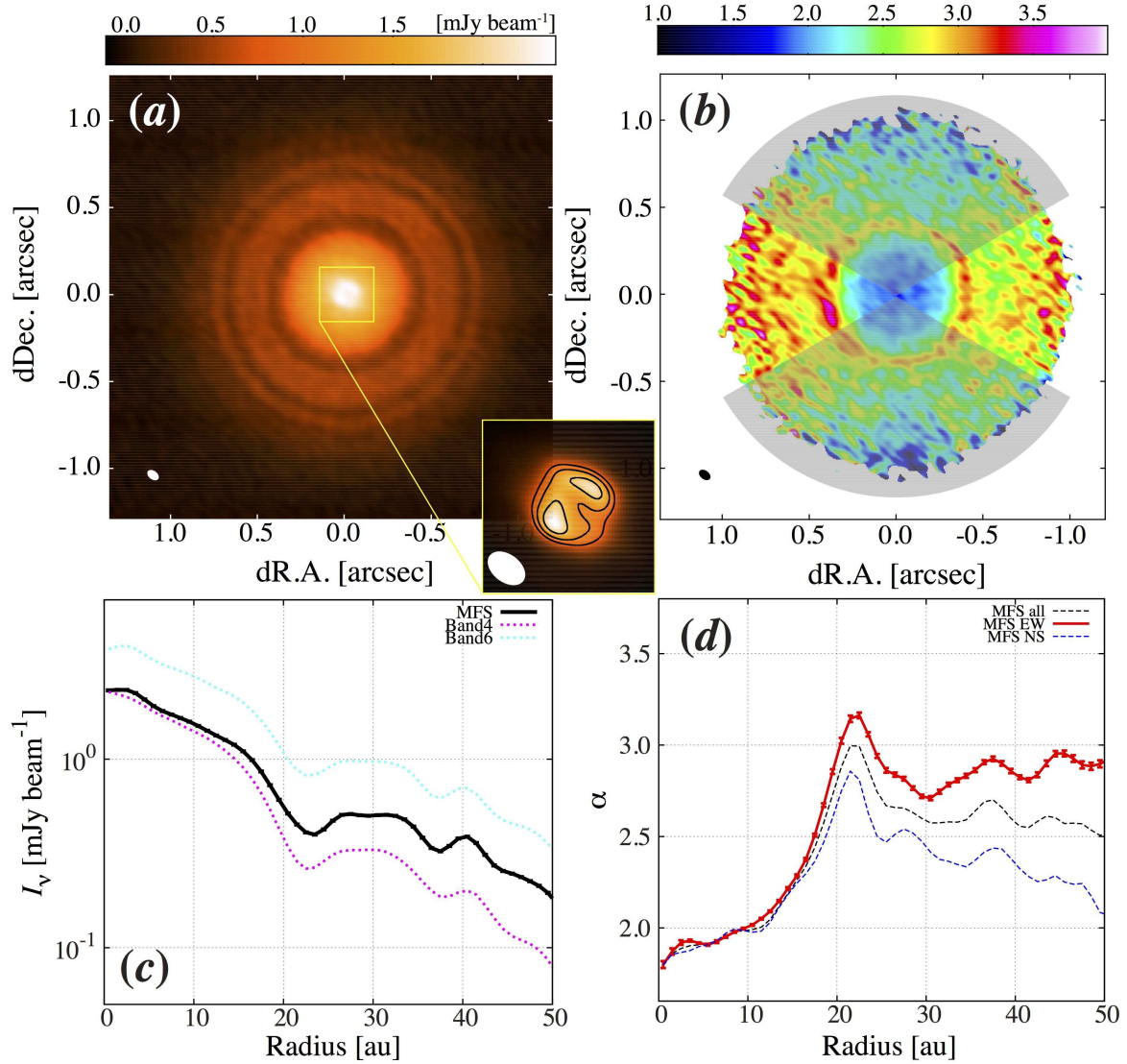


Figure 1. (a) Combined image of bands 4 and 6 with the MFS method. The ellipse at the bottom-left corner shows the synthesized beam. Inset shows a close-up view ($0''.3 \times 0''.3$) for emphasis of the central structure. The contour indicates 130, 140, and 150σ . (b) Spectral index map derived from the MFS method. The shadowed area indicates where the value of the spectral index is unreliable due to the inner hole of the uv coverage. (c) Radial profiles averaged over full azimuthal angle. The flux density of MFS is shown in black and those of bands 4 and 6 data are shown in magenta and cyan, respectively. The error bar shows the standard error through the azimuthal averaging. (d) Radial profiles of the spectral index α . The black line shows the profile averaged over the entire azimuth. The red and blue lines are the profile along the east-west (azimuth angle of $60\text{--}120^\circ$ and $240\text{--}330^\circ$) and north-south ($-30\text{--}30^\circ$ and $150\text{--}210^\circ$) directions, respectively. The error bar follows the same manner as in (c).

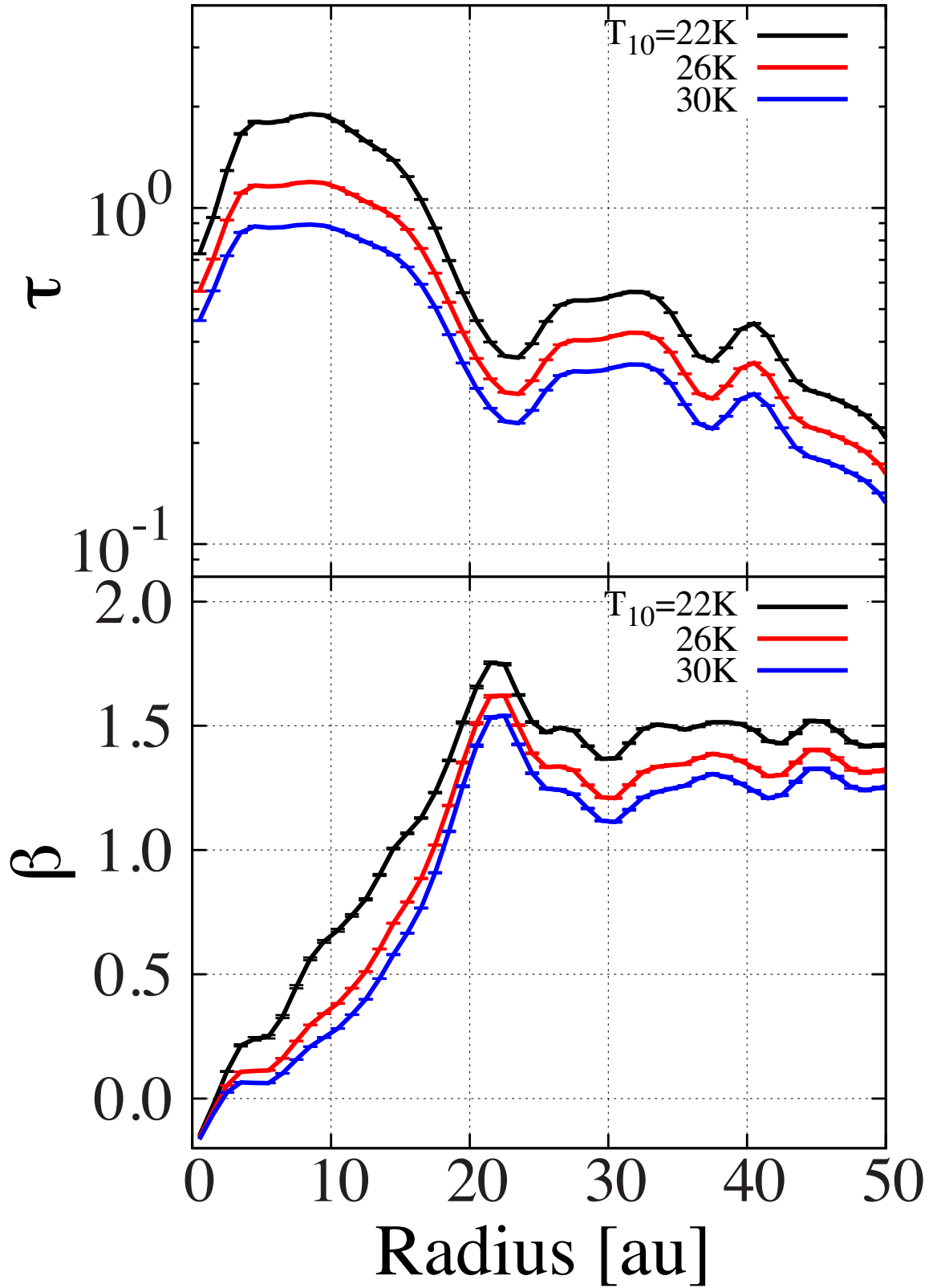


Figure 2. Radial profile of the optical depth at 190 GHz (top) and β (bottom). The cases for $T_{10} = 22, 26, 30$ K are shown in black, red, and blue lines, respectively. The error bar is estimated by using the standard error of the radial profile of the intensity and α shown in Figure 1.

To investigate the uncertainty of the parameters, we assume several values of g and obtain the best-fit gap parameters by the least square method for each value of g . The fit is restricted within $R < 42$ au since it is difficult to model the drop in $\tau(R)$ at larger radii (see below).

Table 3 shows the best-fit parameters with different values of g and T_{10} and figure 3 shows several examples: $g = 1.1$ and 1.2 with $T_{10} = 22$ K, $g = 1.1$ with $T_{10} = 26$ K, and $g = 1.0$ with $T_{10} = 30$ K. The overall trend of the radial variation of $\tau(R)$ is well reproduced. The locations of the gaps, r_g , are well constrained for both gaps and the width of the 22 au gap is also well constrained while the uncertainty of the width of the 37 au gap is large. The depths of the 22 au gap and 37 au gap are determined within typical uncertainties of $\sim 9\%$ and $\sim 43\%$, respectively. It is debatable whether the 37 au feature should be regarded as a gap but it may alternatively be interpreted as a part of radial sinusoidal variation, rather than a single, isolated gap. In some cases where g is varied, the fit to the 37 au gap fails.

We see that the radial profile of $\tau(R)$ drops rapidly at $R \gtrsim 42$ au, and it is difficult to fit the profile with a single background power law. [Hogerheijde et al. \(2016\)](#) show that the radial surface density distribution is well represented by a broken power-law, with the break at ~ 47 au and the steep cutoff ($\propto R^{-8}$) at outer radii. Our results are, at least qualitatively, in agreement with this model and also our previous observations at band 7 ([Nomura et al. 2016](#)).

To investigate whether there are additional, weak structures other than the inner hole, 22 au gap, and 37 au gap, we reconstructed the sub-mm image using radiative transfer calculations. We assume the temperature profile with $T_{10} = 22$ K, and use the best-fit $\tau(R)$ profile with $g = 1.1$ to reconstruct a surface density profile. We assume a dust opacity of $1.9 \text{ cm}^2 \text{ g}^{-1}$ ([Draine 2006](#)) throughout the disk to convert the optical depth to dust density. The dust particles are vertically distributed with a Gaussian profile, with a dust scale height of $H_d(R) = 0.6 \text{ au}(R/10 \text{ au})^{5/4}$. The disk inclination is assumed to be 7° and the major axis position angle is -30° ([Qi et al. 2004](#); [Nomura et al. 2016](#)). This

simple model is constructed based on the parameters used in previous studies (Andrews et al. 2012) except for the newly derived surface density profile having gaps. The main purpose of the modeling is to reproduce the overall observed profile at $R < 42$ au and to find small scale structures that may be hidden behind the conspicuous multiple gap structures.

Figure 4 shows the comparison between the model and observations. The model reproduces the observations between $5 < R < 42$ au. Detailed modeling of the inner hole and outer cutoff is necessary to reproduce the full profiles. At $5 \text{ au} < R < 42 \text{ au}$, the differences between the model and the observations are within $\sim 5\sigma$ in the image. However, if we take the azimuthal average of the residuals, we find a wave like radial profile, with wavelengths of 5–10 au and an amplitude of a few %. This might indicate the presence of sinusoidal distribution of dust particles underlying the gap profiles. To check whether the CLEAN method causes an artificial wave structure, we created the simulated visibility of the model image using the CASA *simobserve* task with appropriate parameters and reconstructed the CLEANed image. The difference of the radial profiles between the simulated observations and the model is also plotted in figure 4(c) and shows no significant sinusoidal pattern like the observed data.

4.2. Origin of the Gaps and Sinusoidal Patterns

The 22 au gap parameters seem to be well constrained with a width of $w_g \sim 4\text{--}5$ au and a depth of $10^{A_g} \sim 0.4\text{--}0.5$ compared to the background τ_{bg} profile. In our previous studies with a spatial resolution of $\sim 0''.35$ (Nomura et al. 2016), the existence of the 22 au gap is hinted at a width of 15 au and a depth of 0.23. The mass deficit within this gap is $1.4 M_J$, assuming a dust mass opacity of $1.9 \text{ cm}^2 \text{ g}^{-1}$ at 190 GHz (Draine 2006) and a gas-to-dust mass ratio of 100, and is consistent between the two observations.

One possible origin of the 22 au gap is planet-disk interaction. Our results for β , which indicates a

mm-sized grain deficit inside the 22 au gap, strongly support this scenario because it is consistent with the picture of dust filtration due to a planet (Zhu et al. 2012). Using the relationship that connects the gap shape with the planet mass (Kanagawa et al. 2015, 2016), a planet with $1.5 M_{\text{Neptune}}$ may be responsible for the gap, assuming a viscosity parameter $\alpha = 10^{-3}$ and a disk aspect ratio of 0.05 (consistent with the assumption of $T_{10} = 22$ K). We note that similar values are derived from both gap width and depth. This planet mass should be considered as the upper limit since the formula by Kanagawa et al. (2015, 2016) is for the gas gap and the actual dust gap may be wider and deeper than the gas gap due to dust filtration (Zhu et al. 2012).

Alternatively, the multiple ring structure might be related to the snow lines of major volatiles (Zhang et al. 2015; Okuzumi et al. 2016). TW Hya is suggested to have a CO snow line at ~ 30 au (Qi et al. 2013; Schwarz et al. 2016), and our observations identify a bright dust ring near this snow line. This is consistent with the dust ring formation scenario by Okuzumi et al. (2016), in which icy dust aggregates experience sintering, disrupt, and pileup near major snow lines. As noted by Andrews et al. (2016), the 40 au bright ring might correspond to the snow line of N_2 , which has a sublimation temperature slightly lower than that of CO.

If real, the sinusoidal distribution in dust particles may be reminiscent of dynamical instabilities within the disk such as zonal flow patterns driven by MHD turbulence (Johansen et al. 2009), baroclinic instability driven by dust settling (Lorén-Aguilar and Bate 2015), and/or the secular gravitational instability (Youdin 2011; Takahashi & Inutsuka 2014). Different dynamical processes act under different physical conditions and therefore, better constraints on the dust disk physical structures based on high resolution observations at other bands (e.g., Andrews et al. 2016) and constraints of the density and temperature structures of gas component are essential in determining the origin of such structures.

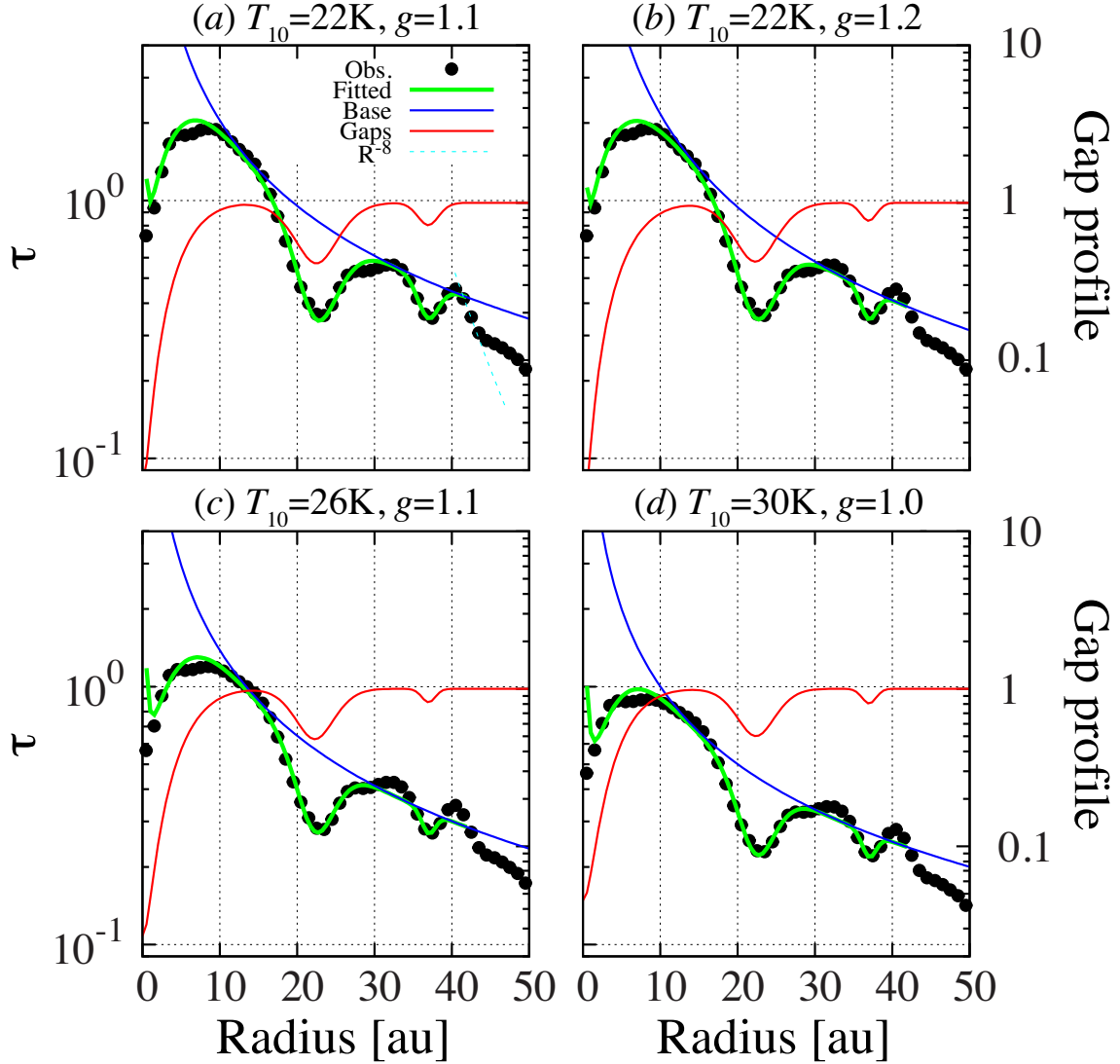


Figure 3. Results of our model fitting (green) for the cases of $g = 1.1$ and 1.2 with $T_{10} = 22$ K (a,b), $g = 1.1$ with $T_{10} = 26$ K (c), and $g = 1.0$ with $T_{10} = 30$ K (d). The black circles indicate the observed data. The blue line indicates the fiducial (background) power-law profile. The profile of each gap is shown in red, whose axis is on the right. The dotted line in cyan in the top-left panel shows the R^{-8} dependence determined by [Hogerheijde et al. \(2016\)](#).

This paper makes use of the following ALMA data: ADS/JAO.ALMA#2015.A.00005.S and ADS/JAO.ALMA#2012.1.00422.S. ALMA is a partnership of ESO (representing its member states), NSF (USA) and NINS (Japan), together with NRC (Canada), NSC and ASIAA (Taiwan), and KASI (Republic of Korea), in cooperation with the Republic of Chile. The Joint ALMA Observatory is operated by ESO, AUI/NRAO and NAOJ. A part of data analysis was carried out on common use

Table 1. Parameters of the fitted inner hole and gaps. The error shows the standard error of the fitting. The systematic error when T_{10} and g are varied is shown at the bottom row.

| Assumed | | | Inner hole | | | 22 au gap | | | 37 au gap | | |
|---|-----|-----------------|------------------|-------|---------------|------------------|----------------|---------------|------------------|----------------|---------------|
| T_{10} | g | τ_0 | A_g | r_g | w_g | A_g | r_g | w_g | A_g | r_g | w_g |
| [K] | | | | [au] | [au] | | [au] | [au] | | [au] | [au] |
| 22 | 1.1 | 2.04 ± 0.03 | -1.78 ± 0.06 | 0 | 6.6 ± 0.1 | -0.39 ± 0.03 | 22.5 ± 0.2 | 4.7 ± 0.3 | -0.14 ± 0.05 | 36.9 ± 0.4 | 2.0 ± 0.7 |
| 22 | 1.2 | 2.17 ± 0.04 | -2.02 ± 0.07 | 0 | 7.2 ± 0.1 | -0.37 ± 0.03 | 22.3 ± 0.2 | 4.6 ± 0.3 | -0.12 ± 0.05 | 36.9 ± 0.5 | 1.5 ± 0.7 |
| 26 | 0.9 | 1.24 ± 0.02 | -1.25 ± 0.04 | 0 | 5.9 ± 0.1 | -0.34 ± 0.03 | 22.7 ± 0.2 | 4.4 ± 0.4 | -0.14 ± 0.04 | 37.0 ± 0.5 | 2.4 ± 0.7 |
| 26 | 1.0 | 1.30 ± 0.02 | -1.40 ± 0.04 | 0 | 6.5 ± 0.1 | -0.33 ± 0.03 | 22.5 ± 0.2 | 4.1 ± 0.4 | -0.12 ± 0.05 | 37.0 ± 0.5 | 1.6 ± 0.8 |
| 26 | 1.1 | 1.38 ± 0.03 | -1.57 ± 0.04 | 0 | 7.1 ± 0.1 | -0.32 ± 0.03 | 22.3 ± 0.2 | 4.0 ± 0.4 | -0.09 ± 0.06 | 37.0 ± 0.7 | 1.3 ± 0.9 |
| 30 | 0.8 | 0.91 ± 0.02 | -1.06 ± 0.03 | 0 | 5.6 ± 0.1 | -0.33 ± 0.03 | 22.8 ± 0.2 | 4.4 ± 0.4 | -0.14 ± 0.04 | 37.2 ± 0.6 | 3.2 ± 0.8 |
| 30 | 0.9 | 0.95 ± 0.02 | -1.20 ± 0.03 | 0 | 6.1 ± 0.1 | -0.31 ± 0.03 | 22.5 ± 0.2 | 4.1 ± 0.4 | -0.12 ± 0.05 | 37.0 ± 0.5 | 1.8 ± 0.7 |
| 30 | 1.0 | 1.00 ± 0.02 | -1.34 ± 0.04 | 0 | 6.7 ± 0.1 | -0.30 ± 0.03 | 22.4 ± 0.2 | 3.9 ± 0.4 | -0.09 ± 0.06 | 37.0 ± 0.6 | 1.3 ± 0.9 |
| Systematic error caused by T_{10} and g changes [%] | | | | | | | | | | | |
| | | 29.8 | 19.9 | 0 | 8.4 | 8.4 | 0.8 | 6.1 | 18.5 | 0.2 | 35.3 |

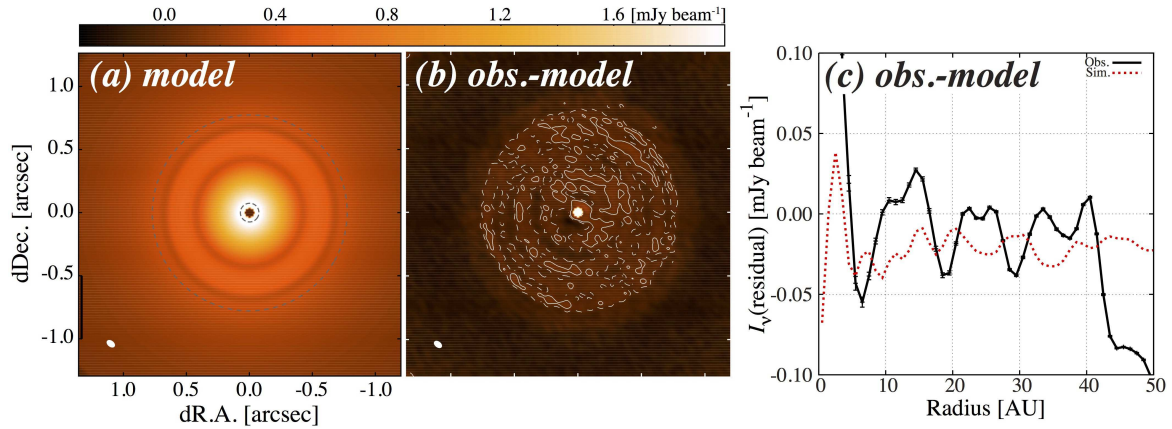


Figure 4. (a) Expected intensity map of the fitted model for the case of $T_{10} = 22$ K and $g = 1.1$. Radii of 4 and 42 au are marked by dotted circles in gray. (b) Residual map after subtraction of the model from the observed data. The solid and dashed contours indicate 3σ and -3σ noise levels of the observed data ($1\sigma = 15.7 \mu\text{Jy beam}^{-1}$). (c) Deprojected radial profile of the residual map (black). The error bar shows the standard error of the observed data. The dotted line in red shows the difference between the CLEANed image, which is created from the simulated visibility, and the original model image.

data analysis computer system at the Astronomy Data Center of NAOJ. This work is partially supported by JSPS KAKENHI grant numbers 24103504 (TT), 23103005 and 25400229 (HN), 26800106 and 15H02074 (TM), and 16K17661 (SO). KDK was supported by Polish National Science Centre MAESTRO grant DEC- 2012/06/A/ST9/00276. Astrophysics at QUB is supported by a grant from the STFC.

Facilities: Atacama Large Millimeter/Submillimeter Array

REFERENCES

- Akiyama, E., Muto, T., Kusakabe, N., et al. 2015, *ApJL*, 802, L17
- ALMA Partnership, Brogan, C. L., Pérez, L. M., et al. 2015, *ApJL*, 808, L3
- Andrews, S. M., Wilner, D. J., Hughes, A. M., et al. 2012, *ApJ*, 744, 162
- Andrews, S. M., Wilner, D. J., Zhu, Z., Birnstiel, T., Carpenter, J. M., Pérez, L. M., Bai, X. N., Öberg, K. I., Hughes, A. M., Isella, A., & Ricci, L. 2016, *ApJL*, 820, L40
- Bergin, E. A., Cleeves, L. I., Gorti, U., et al. 2013, *Nature*, 493, 644
- Calvet, N., D'Alessio, P., Hartmann, L., et al. 2002, *ApJ*, 568, 1008
- Draine, B. T. 2006, *ApJ*, 636, 1114
- Hogerheijde, M. R., Bekkers, D., Pinilla, P., et al. 2016, *A&A*, 586, A99
- Johansen, A., Youdin, A., & Klahr, H. 2009, *ApJ*, 697, 1269
- Kanagawa, K. D., Muto, T., Tanaka, H., et al. 2015, *ApJL*, 806, L15
- Kanagawa, K. D., Muto, T., Tanaka, H., et al. 2016, *arXiv:1603.03853*
- van Leeuwen, F. 2007, *A&A*, 474, 653
- Lin, D. N. C., & Papaloizou, J. 1979, *MNRAS*, 186, 799
- Lorén-Aguilar, P., Bate, M. R. 2015, *MNRAS*, 453, L78
- Muto, T., Grady, C. A., Hashimoto, J., et al. 2012, *ApJL*, 748, L22
- Nomura, H., Tsukagoshi, T., Kawabe, R., et al. 2016, *ApJL*, 819, L7
- Okuzumi, S., Momose, M., Sirono, S.-i., Kobayashi, H., & Tanaka, H. 2016, *ApJ*, 821, 82
- Pérez, L. M., Carpenter, J. M., Chandler, C. J., et al. 2012, *ApJL*, 760, L17
- Pinilla, P., Benisty, M., Birnstiel, T., et al. 2014, *A&A*, 564, A51
- Pinte, C., Dent, W. R. F., Ménard, F., Hales, A., Hill, T., Cortes, P., de Gregorio-Monsalvo, I., 2016, *ApJ*, 816, 25
- Qi, C., Ho, P. T. P., Wilner, D. J., et al. 2004, *ApJL*, 616, L11
- Qi, C., Öberg, K. I., Wilner, D. J., et al. 2013, *Science*, 341, 630
- Schwarz, K. R., Bergin, E. A., Cleeves, L. I., et al. 2016, *arXiv:1603.08520*
- Takahashi, S. Z., & Inutsuka, S.-i. 2014, *ApJ*, 794, 55
- Tamayo, D., Triaud, A. H. M. J., Menou, K., & Rein, H. 2015, *ApJ*, 805, 100
- Tsukagoshi, T., Momose, M., Hashimoto, J., et al. 2014, *ApJ*, 783, 90
- Youdin, A., 2011, *ApJ*, 731, 99
- Zhang, K., Blake, G. A., & Bergin, E. A. 2015, *ApJL*, 806, L7
- Zhu, Z., Nelson, R. P., Dong, R., Espaillat, C., & Hartmann, L. 2012, *ApJ*, 755, 6